Recovering solar fuels from photocatalytic CO_2 reduction over W^{6+}-incorporated crystalline g-C_3N_4 nanorods by synergetic modulation of active centers

Yujie Liang, Xi Wu, Xueyan Liu, Chuanhao Li, Shengwei Liu [*]

School of Environmental Science and Engineering, Guangdong Provincial Key Laboratory of Environmental Pollution Control and Remediation Technology, Sun Yat-sen University, Guangzhou 510006, PR China

ABSTRACT

Graphitic carbon nitride (g-C_3N_4) is promising for photocatalytic conversion of greenhouse gas CO_2 into valuable solar fuels. Crystalline g-C_3N_4 (CCN) attracts great attention, nevertheless, the CO_2 reduction efficiency and selectivity are still dissatisfying, due to the lack of suitable active sites. In this study, tungsten doped CCN (CCN-W) is constructed by forming W-N_6 bonding at the cavity sites of adjacent heptazine units. Significantly, relative to CCN, the full-spectrum CO_2 reduction rate (11.91 μmol g^{-1} h^{-1}) on CCN-W is increased by > 5 times, meanwhile, the photoelectron selectivity to hydrocarbons (CH_4 and C_2H_4) approaching 83% is increased by > 2 times. The W^{6+}-doping introduced W-N_6 as multifunctional active sites enrich both the photoelectrons and CO_2 molecules, and catalyze their selective conversion into hydrocarbons by reducing reaction barrier and moderately stabilizing CO intermediates. This study will offer new insight into modulating the CCN photocatalysts with multifunctional active sites for efficient and selective photocatalytic CO_2 reduction.

1. Introduction

Artificial photosynthesis, based on semiconductor photocatalytic CO_2 reduction, is a promising way for converting CO_2 to hydrocarbons and other solar fuels utilizing clean solar energy [1]. It will not only contribute to mitigate CO_2 emission and to reduce the threat of greenhouse effect to global climate change, but also provide alternative solution to convert and store intermittent solar energy as transportable chemical energy [2]. In the past decades, polymeric graphitic carbon nitride (g-C_3N_4) were intensively studied as a promising visible light responsive metal-free photocatalyst for diverse photocatalytic applications, including artificial photosynthesis [3]. It has attracted extensive attention because of its excellent properties such as intriguing 2D layered structures, well-matched band structures, strong chemical and thermal stability, and cost-effective synthesis.[4] However, the traditional bulk g-C_3N_4 (BCN) always presents amorphous structure (or lower degree of crystallinity), abundant defects, low specific surface area, insufficient solar absorption, and moderate photocatalytic activity, owing to the limited mobility and incomplete polymerization of the nitrogen-containing precursors and/or reaction intermediate during conventional thermal pyrolysis synthesis processes [5]. In particular, it

is widely accepted that, in the amorphous/ill-crystallized g-C_3N_4 structure, neighboring 1D polymeric heptazine chains bridged by hydrogen bonds are terminated with massive residual amino groups, which would act as the charge recombination centers and hinder the charge transfer across the 2D polymer plane [6]. Meanwhile, the interlayer interaction mediated by Van der Waals force is quite weak and the interlayer distance of BCN is relatively large, hindering the interlayer charge transport.

To tackle these problems, a variety of routes including molten-salt method, [7] microwave method, [8] and other routes [9] have been developed to synthesize highly crystalline carbon nitride (CCN). Especially, the convenient molten-salt methods are widely adopted,[10] in which molten salts are used as the high temperature solvent to greatly accelerate mass transfer for the condensation and crystallization process. The higher crystallinity and lower defects in CCN help to reduce bulk charge recombination and accelerate charge transfer. First, the higher degree of covalent polymerization of neighboring heptazine units and the removal of terminal amino groups would facilitate intralayer charge transfer across the 2D π-conjugated plane in CCN [6]. Second, the CCN has a shorter interlayer distance and stronger interlayer interaction than typical BCN, which would decrease interlayer potential barrier and

improve the interlayer charge transfer [11]. In addition, the CCN prepared by molten-salt method usually evolves as nanorod growing along the c axis, which would be beneficial for radial charge transfer to lateral edge surface with much shorter migration distance [12]. Last but not least, the CCN prepared by molten-salt method usually introduces a certain amount of K^+-doping and edge cyano groups,[13] which is also helpful in promoting the charge transfer of CCN. Moreover, CCN always demonstrates much stronger light absorption capacity, due to shorter interlayer distance and stronger interlayer interaction [14]. These advantages of CCN significantly improve its photocatalytic performances for diverse photocatalytic applications [7,12,15]. Despite great progresses, the improvements in photocatalytic performances of CCN for CO_2 reduction are still dissatisfying. Especially, the product selectivity of CCN is seldomly tuned, the main photocatalytic CO_2 reduction product over unmodified CCN is still limited to CO, similar to BCN. It is a challenging but meaningful task to manipulate the microstructures and physicochemical properties of CCN, for example, by defect engineering [16], tuning the conjugated subunits (tri-s-triazine (heptazine) or triazine)[13], heteroatom incorporation[17], and HCl posttreatment [18], and to further optimize the photocatalytic CO_2 reduction performances.

The major challenge lies in that the electron accumulation centers, CO_2 adsorption centers and reduction reaction centers on g-C_3N_4 are spatially disordered [19]. As is well documented, the valence band (VB) of g-C_3N_4 is occupied by N 2p orbital, while the conduction band (CB) is mainly composed of C 2p and N 2p orbital [20]. N 2p orbital contribute to both CB and VB. In this regard, the charge carriers and the redox centers cannot be well spatially separated. The photogenerated holes and electrons would be easily recombined, and the redox reactions would interfere with each other. Specifically, the CO_2 adsorption centers on g-C_3N_4 is usually located around N-sites with Lewis alkalinity. The photoelectron-dominated CO_2 reduction reaction on N-sites would be compromised by surrounding photogenerated holes, and CO_2 reduction products would be re-oxidized by surrounding photogenerated holes, especially taking account of the relatively inferior oxidation potential of holes from VB of g-C_3N_4, relative to water oxidation potential. To meet this challenge, it is crucial to introduce additional multifunctional synergetic active sites, to spatially separate the photogenerated electrons and holes, and to match the reduction and oxidation centers accordingly. Xiang et al. successfully incorporate single Cu atom in CCN, [17] acting as active sites where the photoelectrons are accumulated and the CO_2 reactants are adsorbed. It largely promotes the activation and reduction of CO_2 to CO efficiently and selectively. In addition, it is reported that the nitrogen vacancies (N_v) in CCN can also trap and activate CO_2 molecules [21]. However, up to now, the main CO_2 reduction products over reported unmodified and modified CCN are still limited to CO (two-electron reduction product). Incorporating active site capable of storing photoelectrons trapped would be important for the production multi-electron reduction products. Owing to the reversible chemical state change of tungsten (W) component (W^{6+}/W^{5+} cycle) and intriguing electron storage properties of W-species (e.g. WOx), [22] W^{6+}-doping are widely adopted to promote the capture and storage of photoelectrons [23]. It is expected that the W^{6+}-doping induced electron accumulation and storage would not only suppress the charge recombination and promote charge dynamics, but would also improve CO_2 reduction selectivity to multi-electron reduction products. In contrast, K^+-doping usually doesn't give rise to the localized levels within the band gap, and doesn't have the ability to store photoelectrons [24]. In addition, recent researches on supported single-atom catalysis indicated that MNx (M= W, Mo, Cu etc.) based active centers with unique M-N bonding would significantly modulate the reaction efficiency and selectivity [25,26]. For example, it is reported that MoN_2 sites favor the selective and efficient photocatalytic CO_2 conversion into hydrocarbon products [26]. Cao et al. present that C-Cu-N_2 single-atom catalytic sites effectively collect the photogenerated electrons for CO_2 activation and reduce the energy barrier of CO_2 reduction reaction [27]. Considering

that the lone pair of electrons on nitrogen atoms could be used to stabilize transition metal atom as Lewis basic sites, g-C_3N_4 is an excellent matrix providing abundant and uniform nitrogen coordinators to anchor W^{6+}-dopant [28]. Based on theoretical calculation, Chen et al. found that the six-fold cavity of g-C_3N_4 is energetically the most favorable site for anchoring W-atom [29]. Inspired by these studies, it is reasonable that subtle doping g-C_3N_4 with W^{6+} and introducing unique W-N_6 bonding would not only promote the targeted electron accumulation, but also modulate the directional electron-dominated reactions, together leading to improved CO_2 reduction efficiency and selectivity.

In this study, using preformed CCN as precursor and $W(CO)_6$ as the metal source, W^{6+}-doped crystalline carbon nitride (CCN-W) nanorods involving W-N_6 bonding are prepared with the assistance of solvothermal treatment. It is revealed that W-N_6 bonding in CCN-W is formed by coordinating lone pair electrons of N 2p at cavity site of adjacent heptazine units with the vacant orbital of W^{6+} ions. As expected, the electron storage capability of W^{6+} favors the trapping and accumulation of photoelectrons on W-N_6 moiety, suppressing the charge recombination. Meanwhile, W-N_6 centers in CCN-W facilitates the chemisorption CO_2 and CO intermediates with moderate coverage and intensity. As a consequence, the accumulated photoelectrons and adsorbed CO_2 meeting at W-N_6 centers would efficiently reduce to CO intermediate, which undergo further hydrogenation to generate hydrocarbons (CH_4 and C_2H_4) with high selectivity of about 83%. Besides, due to W^{6+}-doping, the band structures of CCN-W are tuned. The visible light absorption capacity is enhanced by forming localized levels in the band gap. Meanwhile, the hole oxidation potential and H_2O oxidation dynamics are enhanced by lowering VB edge position.

2. Experimental section

2.1. Fabrication of tungsten doped crystalline carbon nitride (CCN-W) nanorods

CCN nanorods were firstly synthesized by a typical molten-salt approach [12]. The tungsten doped CCN (CCN-W) photocatalyst was then fabricated by a facile solvothermal assisted post-processing strategy using $W(CO)_6$ as doping agent. For comparison, BCN was also prepared by conventional thermal pyrolysis method [30], and WO_{3-x} was prepared by similar solvothermal method [31]. More details on the synthesis of CCN-W, BCN, CCN and WO_{3-x} samples were elaborated in Text S1 in the Supporting information.

2.2. Characterizations

The multileveled compositions and structures of as-prepared samples are characterized by X-ray diffraction (XRD) patterns, X-ray photoelectron spectroscopy (XPS), Fourier transform infrared spectroscopy (FTIR), Electron paramagnetic resonance (EPR) spectroscopy, scanning electron microscopy (SEM), transmission electron microscopy (TEM), high-resolution transmission electron microscopy (HRTEM), high angle annular dark field (HAADF)-scanning TEM (STEM) and energy-dispersive X-ray spectroscopy (EDS) elemental mappings. The pore features and adsorption properties are measured using nitrogen sorption isotherms, CO_2 adsorption curves, CO_2, CO, or O_2-based temperature programmed desorption (TPD) curves. The optical properties were analyzed by UV–vis diffuse reflectance spectroscopy (UV–vis DRS), steady state photoluminescence (PL) spectra and time-resolved PL spectra. The electrochemical and photoelectrochemical properties are analyzed in terms of the transient photocurrent response, electrochemical impedance spectra (EIS), and linear sweep voltammetry (LSV) curves. More details were elaborated in Text S2 in the Supporting information.

2.3. Examination of photocatalytic CO₂ reduction performance and mechanism

The water-coupled photocatalytic CO_2 reduction performance was examined by a typical gas-solid interfacial reaction system under anaerobic conditions, similar to our previous studies [30]. The light source is a 300 W Xe arc lamp (PLS-SXE300, Perfectlight, China) without (full spectrum, 320–780 nm), or with different specific filters, including, an UV cutoff filter (visible light, 420–780 nm), an AM 1.5 G filter together with a total reflector (AM 1.5 G, 200–1100 nm), or with diverse band-pass filters to obtain different monochromatic lights (350, 380, 400, 420, 435, 475, 500 nm). The gas products were analyzed using an integrated gas chromatograph (GC-7890B, Agilent) equipped with two flame-ionized detectors (FIDs) and a thermal conductivity detector (TCD). ^{13}C isotope tracer experiment was conducted to verify the carbon source of the reduction products under identical operation conditions. To disclose the photocatalytic CO_2 reduction mechanism on CCN-W surface, the CO_2 adsorption and photocatalytic evolution processes were monitored using the in situ diffuse reflectance infrared Fourier transform spectroscopy (DRIFTS), similar to our previous studies [30]. More details were elaborated in Text S2 in the Supporting information.

## 3. Results and discussion

3.1. Structural and compositional characterizations

The microstructural characteristics of CCN-W nanorods are illustrated in Scheme 1, in comparison with CCN nanorods and BCN. BCN (Scheme 1, left) is characteristic of high density of terminal amino groups and weak interlayer interaction (enlarged interlayer distance) [32]. In contrast, CCN (Scheme 1, middle) has reduced density of terminal amino groups and reduced interlayer distance (strengthened interlayer interactions) [7]. Moreover, as clearly demonstrated previously, K^+-doping and terminal cyano groups are normally introduced into CCN during molten-salt treatment processes [13]. The K^+-doping often present in three positions (Scheme 1): intercalated into the CCN interlayer; doped in the cavity confined by adjacent heptazine units or acting as charge compensator for the terminal cyano/amino groups. K^+-doping is important in tuning the charge transfer dynamics of CCN. The K^+ intercalation induce a unique built-in electric field (BIEF), benefiting the interlayer electron transfer [33]. Meanwhile, the cave K^+

doping introduce new delivery paths for increasing electron delocalization, facilitating the intralayer transfer of photoelectrons between the adjacent heptazine rings [13]. CCN-W are prepared by simply treating as-prepared K^+-doped CCN in the presence of $W(CO)_6$ under solvothermal conditions. As will be further demonstrated later, during the solvothermal treatment process, a portion of tungsten ions (W^{6+}) will replace K^+ in the cavity through ion exchange, forming $W-N_6$ bonding by six-fold coordinating with the surrounding N atoms from the adjacent heptazine units (Scheme 1, right). Meanwhile, a part of incorporated tungsten, existing in the form of tungstate ions (e.g. WO_4^{2-}), enters into the $g-C_3N_4$ interlayer to compensate with intercalated K^+ ions. In addition, because of solvothermal-assisted side by side edge re-polymerization of CCN-W nanorods, the density of edge cyano groups are reduced to some extent, and accordingly, the amounts of compensating K^+ is also reduced. The illustrated microstructural features of CCN-W are further demonstrated below by combining the microscopical and spectrometric characterizations (Figs. 1–3).

The morphology is firstly investigated using SEM images (Fig. 1a, b). As shown in Fig. 1, W^{6+}-doping hardly alter the basic morphology, both CCN and CCN-W are appeared as regular nanorods. The average length of nanorods is around 350 nm and the average diameter is about 70 nm. The microstructures of CCN-W are further investigated by the TEM (Fig. 1c) and HRTEM (Fig. 1d) images. The nanorod-like morphology is well preserved in CCN-W upon solvothermal-assisted W^{6+}-doping treatment. (Fig. 1c). Owing to the high crystallinity, the resolved lattice fringes with spacing of 0.98 nm are recorded for CCN-W, which is corresponding to the interlayer distance along c axis [7]. The elemental compositions and distribution within CCN-W nanorods are further demonstrated by the EDS elemental mappings of C, N, K, W and O (Fig. 1f–j), performing on the corresponding HAADF-STEM image (Fig. 1e). Generally, C, N, K, W and O elements are uniformly distributed in the CCN-W sample, indicating that W-dopant is successfully incorporated, in addition to K and O.

The XRD patterns are used to identify the phase structures of the prepared samples. As shown in Fig. 2a, two diffraction peaks at 13.1° and 27.4° are recorded, matching the typical (100) and (002) crystal planes of intrinsic BCN. The peak at 13.1° is corresponded to the in-plane packing of 1D polymeric heptazine chains and the peak at 27.4° is assigned to the interlayer stacking of 2D π-conjugated plane [34]. In contrast, for CCN, these two peaks are located at 8.0° for (100) and 28.2° for (002), respectively. A significant shift in diffraction peaks suggests
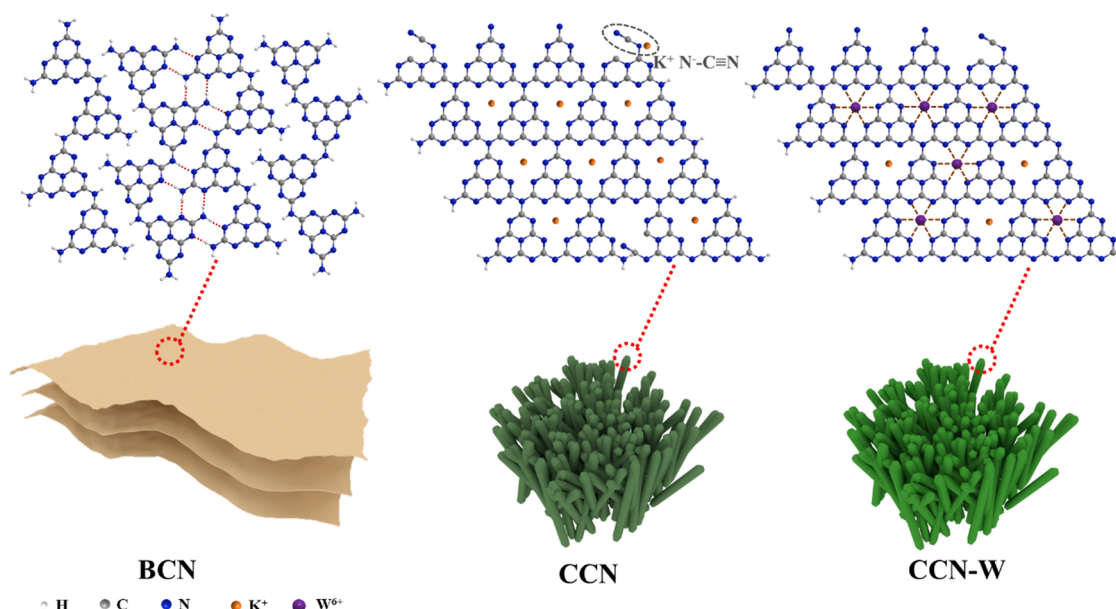
Scheme 1. Schematic diagram of the structural characteristics for CCN-W nanorods, in comparison with BCN nanosheets and CCN nanorods.
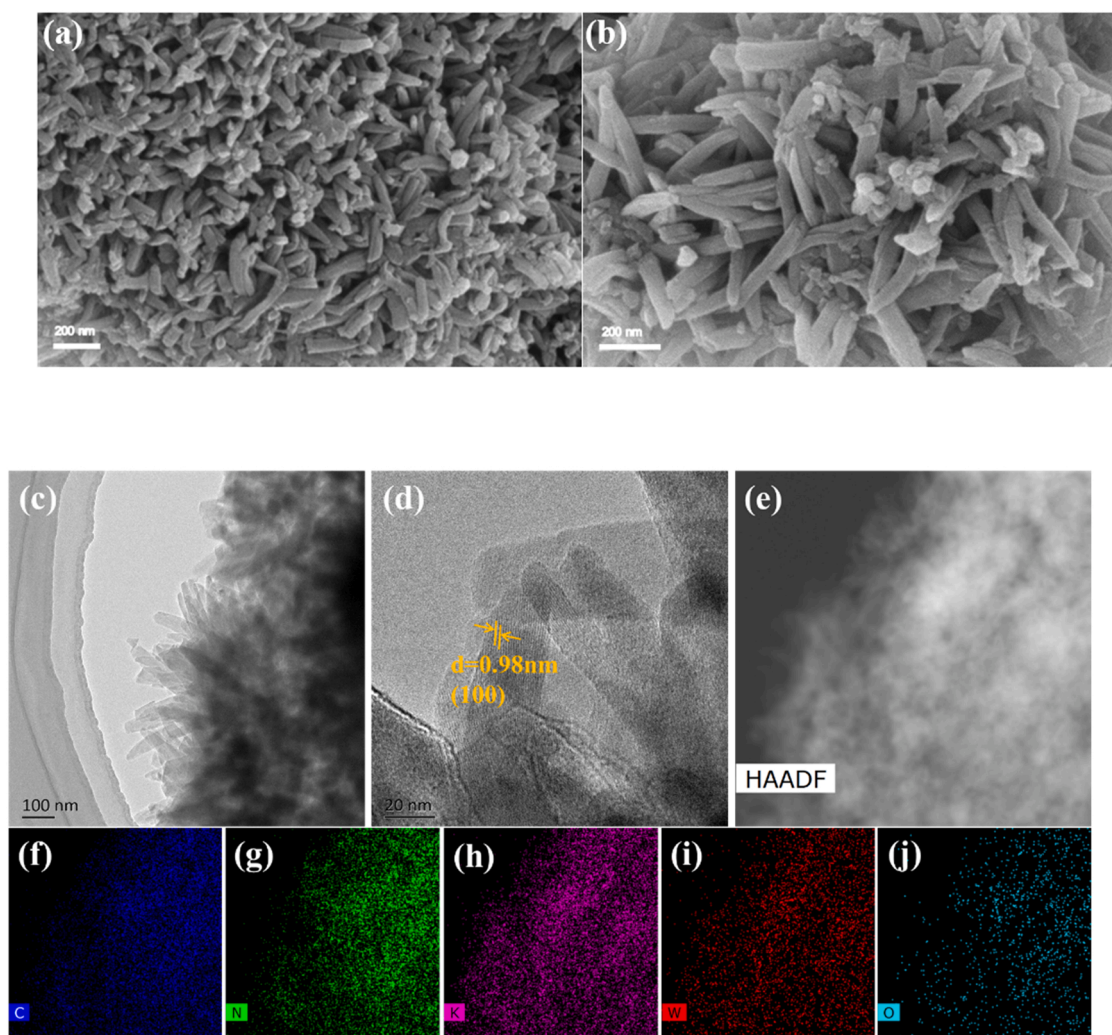
Fig. 1. SEM images of samples CCN (a), CCN-W (b), TEM image (c), HRTEM image (d), HAADF-STEM image (e), and the corresponding EDS elemental mappings (f–j) of the typical sample CCN-W.

the obvious changes in the local microstructures of CCN. The (100) peak is negatively shifted to a much lower angle, corresponding to enlarged distance within in-plane repeating motifs, which is probably originated from cave K^+ doping and unfolded in-plane network associated with the removal of terminal amino groups, and sufficient in-plane covalent condensation of adjacent heptazine rings [7]. In contrast, the (002) peak is otherwise positively shifted from 27.4° to 28.2°, corresponding to a decreased interlayer distance and stronger interlayer interactions [35]. CCN-W shares similar two diffraction peaks as that of CCN. No other resolvable XRD peaks, especially those related to W^{6+}-involving species, are recorded, implying that incorporated W^{6+} is dominantly doped in the g-C_3N_4 framework, but no crystalline impurities like WO_{3-x}, tungsten carbide, or tungsten nitride are introduced into the as-prepared CCN-W sample [36]. In comparison, slight variations in diffraction peaks indeed occur for CCN-W relative to CCN. After W^{6+}-doping and the replacement of K^+ by much larger W^{6+}, the intensity of (100) peak for CCN-W decrease to some extent, implying the increased defect density of N vacancies (N_v) and the decreased local order/periodicity of in-plane packing of heptazine units [37]. Besides, after W^{6+}-doping and the intercalation of WO_4^{2-} into the interlayer, the (002) peak for CCN-W is slightly shifted negatively to a lower angle (27.9°), relative to that for CCN. Accordingly, the calculated interlayer spacing along c axis is expanded from 0.316 nm (CCN) to 0.320 nm (CCN-W), after tungstate ions (WO_4^{2-}) inserting into the g-C_3N_4 interlayer. The phase structures of CCN-W-X (X = 1, 2, 3) are shown in Fig. S1a.

The compositional and structural changes of BCN, CCN and CCN-W are further identified by FTIR spectroscopy (Fig. 2b). All those sample exhibited similar FTIR spectra, meaning that they shared the same basic chemical structures. A broad peak in the region of 3500–2900 cm^{-1} is attributed to the uncondensed terminal amino group or surface hydroxyl groups. Compared with BCN, this peak is obviously weakened for CCN, indicating lesser terminal amino groups, which is attributed to the removal of terminal amino groups and full condensation of adjacent heptazine units in CCN. After solvothermal-assisted W^{6+}-doping, a slight enhancement of this peak for CCN-W versus CCN is possibly related to more surface hydroxyl groups on CCN-W. The bands ranging from 1700 to 1200 cm^{-1} are corresponding to the stretching vibrations of the conjugated CN heterocycles. The typical peak at 810 cm^{-1} is ascribed to the breathing vibration mode of heptazine units.[2] Relatively, these bands become weaker in CCN-W versus CCN, owing to the electronic interaction between the doped W^{6+} ions at the cavity sites and the surrounding N atoms from adjacent heptazine units [36]. In sharp contrast to BCN, a new peak at 2150 cm^{-1} is emerged for CCN, which is ascribed to the edge cyano groups [38]. Those cyano groups are formed by breaking of the 1D polymeric heptazine chains and the opening of the heptazine ring, during molten-salt processes. Those cyano groups are generally stabilized by K^+, involving charge compensation. Accordingly, an accompanying peak, related to terminal cyano groups bound K^+ (that is, K^+-NC_2 group) [7], is appeared at 1000 cm^{-1}. Notably, relative to CCN, both 2150 cm^{-1} peak and 1000 cm^{-1} peak for CCN-W become
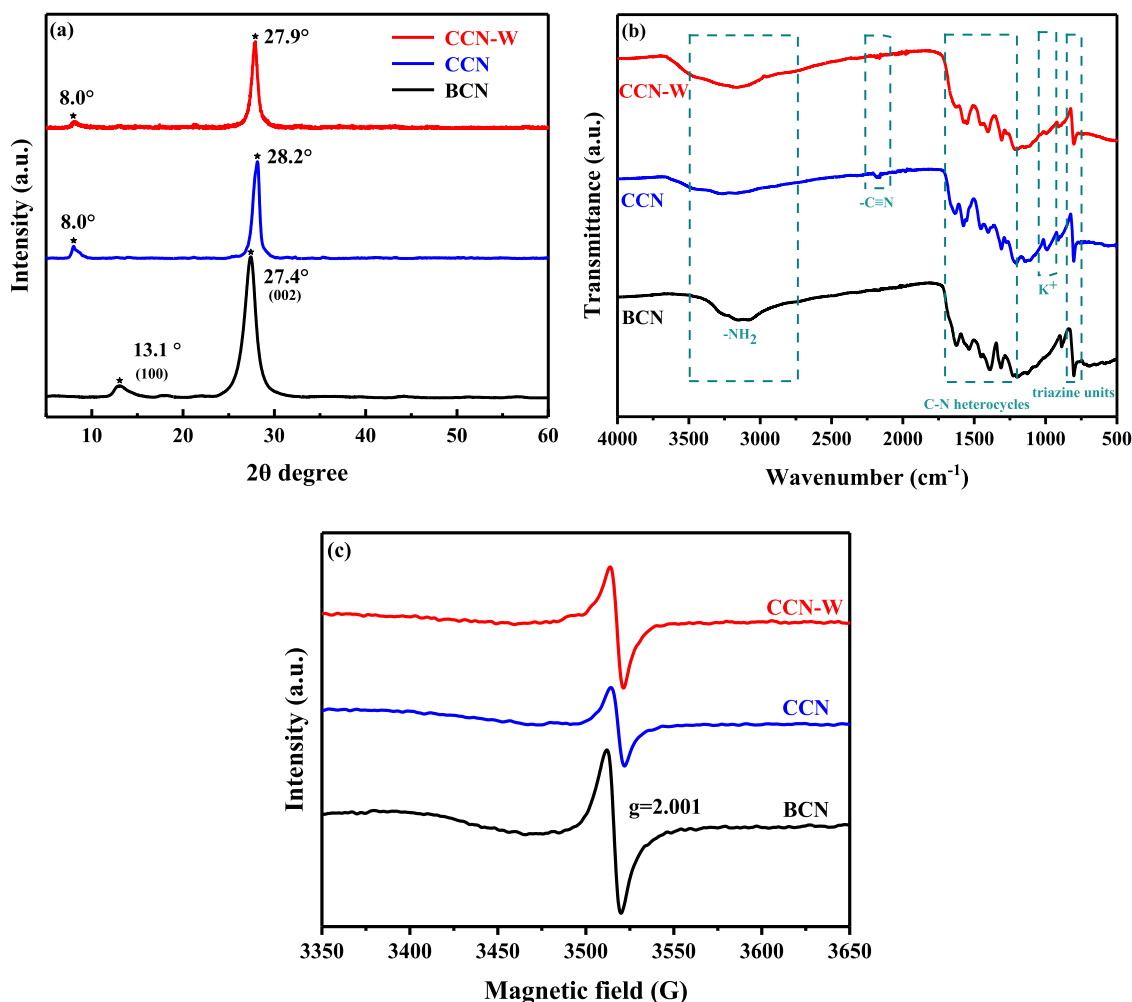
Fig. 2. XRD patterns (a), FTIR spectra (b), and EPR spectra (c) of as-prepared BCN, CCN, and CCN-W.

much weaker, corresponding to the loss of terminal cyano groups together with compensated K^+ in CCN-W. The solvothermal-assisted W^{6+}-doping processes promote the condensation of terminal cyano groups and closure of the heptazine ring, [39] which is further supported by the following XPS result. The samples of CCN-W-X (X = 1, 2, 3) exhibit similar FTIR spectra (Fig. S1b).

EPR spectra (Fig. 2c) is used to investigate the defect states and charge mobility of the samples [40]. All the three samples display a similar EPR peak (g = 2.001), which is related to the unpaired electrons of the sp^2-carbon in the π-conjugated plane [18]. The intensity of this EPR peak is sensitive to the detect density of N_v or the degree of π-electron delocalization. Owing to higher crystallinity and low defect density of CCN, the corresponding EPR peak of CCN is lower than BCN [7]. A low defect density in CCN would reduce exciton recombination possibility and accelerate the exciton dissociation dynamics. Upon W^{6+}-doping, the EPR peak intensity for CCN-W is much stronger than that for CCN. It indicates that the W^{6+}-doping would introduce additional N_v defects and W-N_6 associated the electron localization in the π-conjugated plane [41].

In addition, the surface chemical states of CCN and CCN-W are further identified by XPS spectra. The C 1 s spectrum (Fig. 3b) of CCN contains three components located at 284.8 eV (adventitious carbon), 286.8 eV (terminal cyano groups (-C≡N) or amino groups (C-NH$_x$)) and 288.3 eV (sp^2-hybridized carbon in heptazine rings (N-C≡N)) [16]. A positive shift to higher binding energies occurs at N-C≡N peak for CCN-W (288.4 eV) relative to CCN (288.3 eV), which indicates that W^{6+}-doping into the cavity confined by heptazine rings decreases the

electron density of N-C≡N, suggesting strong electronic interactions between doped W^{6+} and heptazine ring [23]. Meanwhile, due to solvothermal-promoted condensation of terminal cyano groups during W^{6+}-doping, the corresponding -C≡N peak for CCN-W weakens in intensity and shifts negatively in peak position (from 286.8 to 286.3 eV) [42]. The N 1 s spectrum (Fig. 3c) of CCN can be fitted into four peaks positioned at 403.9 eV (π excitation), 401.3 eV (terminal amino groups (-NH$_x$) or terminal cyano groups (-C≡N)), 400.4 eV (tertiary nitrogen (N-(C)$_3$)), and 398.7 eV (nitrogen in heptazine rings (C-N≡C)) [43]. Upon cave W^{6+}-doping, because of strong electron interaction between doped W^{6+} and heptazine ring, a positive shift to higher binding energies occur accordingly at C-N≡C peak for CCN-W (398.8 eV), relative to that of CCN (398.7 eV). The lower electron density of C and N atoms in CCN-W is caused by W^{6+}-doping and forming W-N_6 bonding, in which electrons tend to transfer from N moieties in heptazine ring to empty orbitals of higher valence W^{6+} via Lewis acid-base interaction [37]. It has been demonstrated that the six-fold cavity confined by heptazine rings in g-C$_3$N$_4$ is the energetically most favorable site for anchoring W-atom and forming W-N_6 bonding [29]. The resulting W-N_6 sites would be active centers for both electron storage and electron-dominated catalytic reduction reactions. Note that, the binding energy of N for each component in CCN-W is somewhat higher than that in CCN, suggesting a lower electron density, corresponding to a weaker Lewis basicity and moderate adsorption affinity to CO$_2$. Besides, the C/N atomic ratio in CCN-W is higher than that in CCN (Table S1), which might be caused by the increase in defect density of N_v [43]. Meanwhile, the intensity of N-(C)$_3$ peak is enhanced for CCN-W, confirming the loss
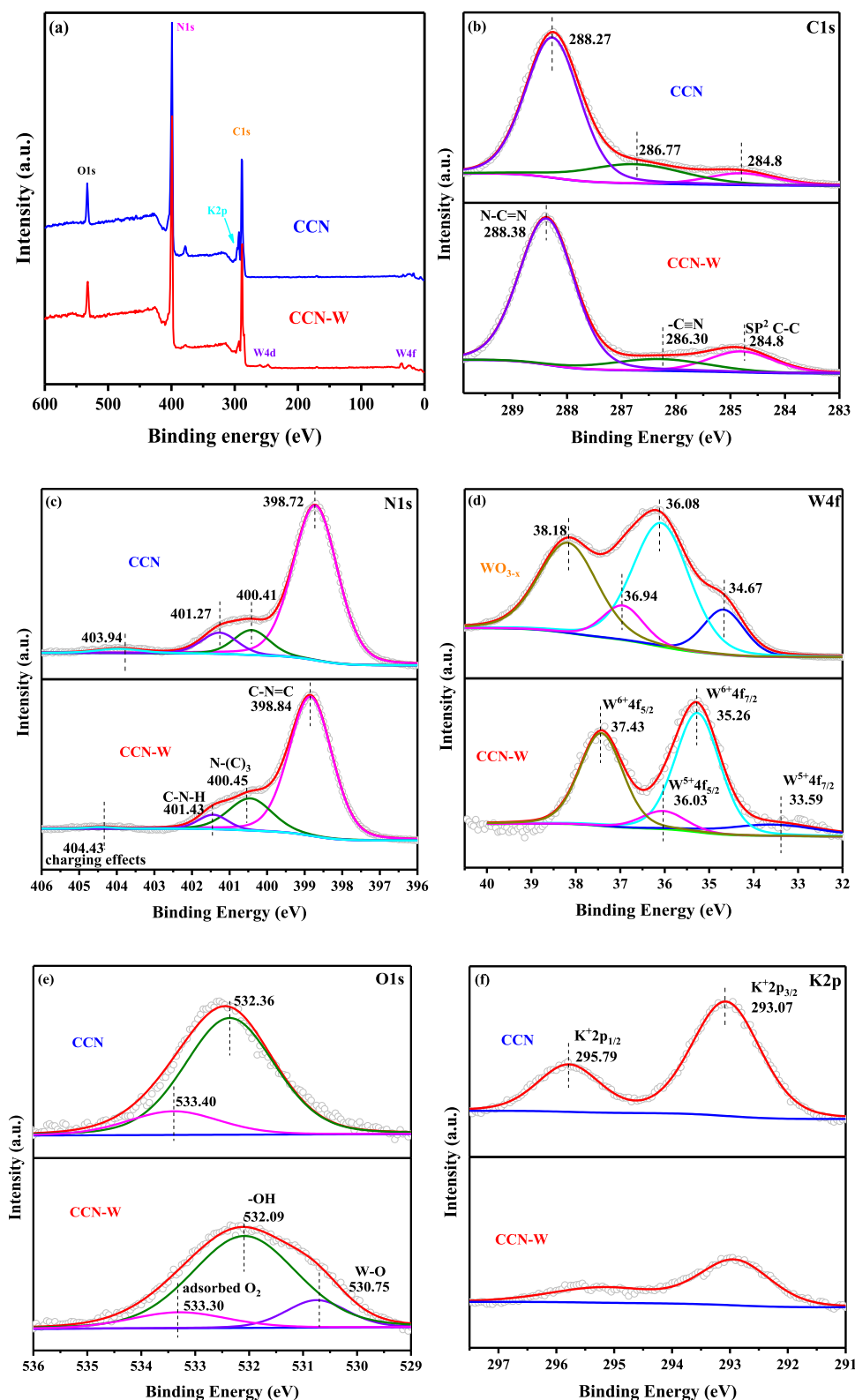
Fig. 3. XPS survey spectrum (a), and high-resolution XPS spectra of C 1 s (b), N 1 s (c), W 4 f (d), O 1 s (e), and K 2 p (f) of CCN and CCN-W.

of terminal amino groups and cyano groups. The solvothermal-promoted re-polymerization would extend π-conjugated plane and promote the intralayer charge mobility.

The two branches of O 1 s spectrum (Fig. 3e) for CCN are related to the surface hydroxyls (-OH) and surface adsorbed O_2 [44,45]. As for CCN-W, in addition to these two components, a new peak is emerged at

binding energy of 530.8 eV, attributing to the W-O-W in tungstate ions (WO_4^{2-}) [46]. The W 4f spectra (Fig. 3d) for CCN-W could be divided into two pairs. The first pair of peaks at 37.4 and 35.3 eV belong to the W^{6+}, and another pair of peaks at 36.0 and 33.6 eV are attributed to the W^{5+} that are derived from the partial W^{6+} reduction as a result of W-N$_6$ bonding and electron transfer [23]. Moreover, the binding energy of

corresponding W^{6+} and W^{5+} peaks in CCN-W are lower than in WO_{3-x}, which is due to the bonding of W^{6+} and W^{5+} to the N atoms with a lower electronegativity than the O atoms [47]. It is clearly that W^{6+}-dopant have been successfully incorporated into the g-C_3N_4 framework of CCN-W, in both the cavity sites and the interlayer space. The reversible change in chemical states of W dopant (W^{6+}/W^{5+} cycle) would be important for the capture and storage of photoelectrons during photocatalytic reactions. The K 2p spectra (Fig. 3f) confirm the K^+ incorporation in both CCN and CCN-W. The K^+-doping amount decreases from 3.18% in CCN to 1.37% in CCN-W (Table S1). Several reasons may account for the decrease in K^+-doping level in CCN-W. First, the ion exchange between W^{6+} and K^+ in the cavity site will lead to a reduce in K^+-doping level. Second, owing to solvothermal-promoted condensation of terminal cyano groups during W^{6+}-doping, the amount of dangling -C≡N or C-NH_x is reduced, and the compensating K^+ ions is thus decreased, [18] being consistent with FTIR spectra.

3.2. Porous structure and adsorption properties

The specific surface area and pore features of the samples are determined by N_2 sorption (Fig. 4a). The N_2 sorption isotherms for CCN and CCN-W are comparable, which show a typical type-IV isotherms with H3-type hysteresis loops [34], corresponding to the mesoporous structures with wide pore size distribution (inset in Fig. 4a). The determined BET surface area (S_{BET}) of CCN and CCN-W are 76.5 and 57.1 m^2 g^{-1}, respectively, both are much higher than that of BCN (11.7 m^2 g^{-1}). Higher S_{BET} generally suggests the exposure of more active sites for reactant adsorption and activation [48,49]. Because of the interfacial side by-side edge condensation of terminal amino/cyano groups and the attachments of adjacent CCN-W nanorods during solvothermal treatments, the S_{BET} and pore volume of CCN-W are slightly decreased, relative to CCN (Table S2).

CO_2 adsorption as the first step of photocatalytic CO_2 reduction reaction is very important. According to the CO_2 adsorption curves in Fig. 4b, in the relative pressure (P/P_0) range of 0.1 – 1, the CO_2 adsorption capacity is almost linearly related to P/P_0 for all the samples. This character suggests that CO_2 molecules are dominantly adsorbed on the samples by physical interaction, and the CO_2 adsorption capacity is mainly affected by S_{BET}. Moreover, in the P/P_0 range of 0–0.1, the CO_2 uptakes are exponentially increased for samples CCN and CCN-W. This phenomenon indicates the existence of chemical adsorption between the two samples and CO_2, which could be further demonstrated by CO_2-TPD analysis (Fig. 4c). CO_2-TPD analysis is used to disclose the chemisorption characteristics and basic sites within the samples. As shown in Fig. 4c, the weak CO_2 desorption peak for BCN is positioned at 76 °C, which is attributed to the desorption of CO_2 adsorbed at the terminal amino groups (C–NH_x) on the surface. Relatively, CCN exhibits much stronger CO_2 adsorption capacity and intensity, presenting two intensive CO_2 desorption peak at much higher temperature. The two desorption peaks located at 159 and 450 °C could be related to two different CO_2 adsorption sites, that are associated with the K^+-doping in CCN. It is reported that the alkaline metal doped in g-C_3N_4 is easy to lose both the outermost electrons and part of the sub-outer electrons, and most of which would transfer to the surrounding N atoms, thus causing the charge redistribution of the surrounding N atoms [24]. Since the conjugated system of the heptazine unit promotes electron delocalization, the basicity promoted by K^+ ions doped in cavity confined by heptazine ring is weaker. In contrast, the K^+ ions compensating with terminal cyano groups could promote the adjacent N atom exhibiting stronger alkalinity. In this regard, it is speculated that the CO_2 desorption peak at 159 °C corresponds to the cave K^+-doping and K-N bonding confined by the heptazine ring, while the CO_2 desorption peak at 450 °C corresponds to the K^+-compensated terminal cyano/amino groups [15]. By comparison, both CO_2 adsorption capacity and intensity for CCN-W are
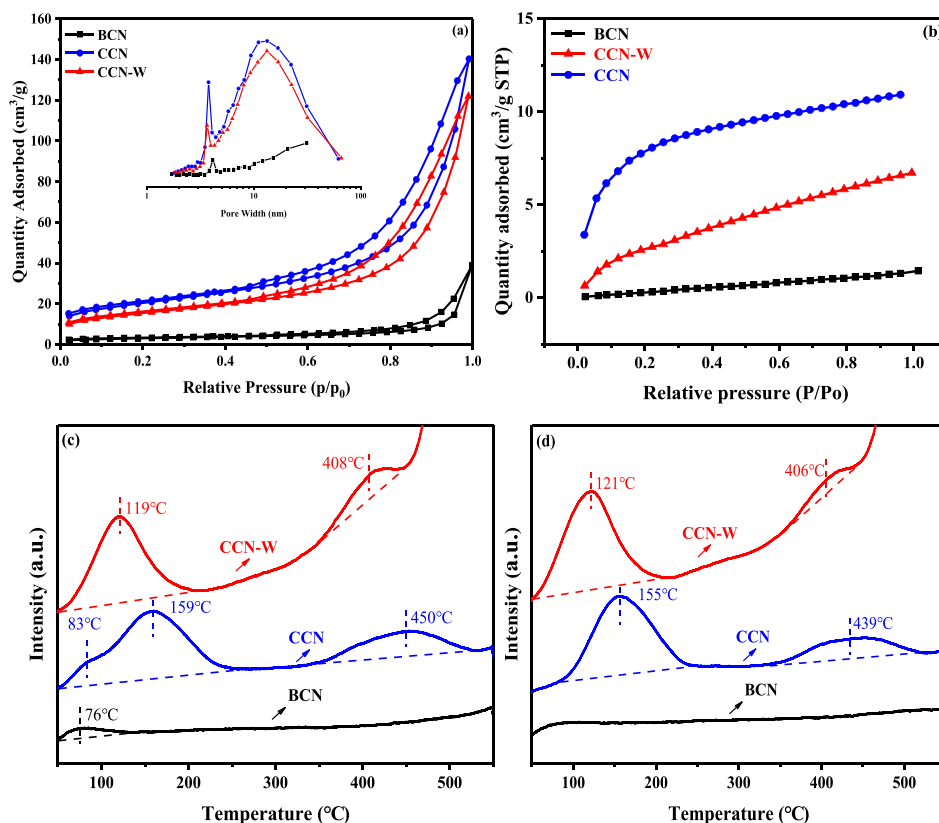

Fig. 4. Nitrogen sorption isotherms (a), CO_2 adsorption curves (b), CO_2-TPD (c) and CO-TPD (d) profiles of samples BCN, CCN and CCN-W. The inset in (a) shows the corresponding pore size distribution profiles.

weakened to some extent. The two CO_2 desorption peaks for CCN-W are centered at about 119 and 408 °C. As demonstrated earlier by FTIR and XPS results, after solvothermal-assisted W^{6+}-doping, the portion of left K^+ is significantly reduced together with the loss of terminal cyano groups. Meanwhile, the basicity of K^+ bounded by terminal cyano groups would be compromised by the charge compensation effects of incorporated WO_4^{2-}. Moreover, the basicity of K-N bonding could be weakened by substituted $W-N_6$ bonding in cavity sites. In fact, the above XPS results also indicate a lower electron density and weaker Lewis basicity of N-moieties in CCN-W because of $W-N_6$ bonding, which would offer moderate adsorption affinity to CO_2. In summary, both the CO_2 adsorption capacity and intensity follows the following order: CCN > CCN-W > BCN. A proper adsorption capacity and strength is usually beneficial for catalytic reactions, facilitating reactant activation and easing product desorption.

CO is an important intermediate towards multi-electron reduction products during photocatalytic CO_2 reduction, and the CO adsorption capacity and intensity largely determine the selectivity to hydrocarbons. According to the CO-TPD results (Fig. 4d), BCN has almost no CO adsorption capacity, favoring the preferential production of CO as major reduction product over BCN. In contrast, considerable CO adsorption is taken place over both CCN and CCN-W. Interestingly, the CO desorption curve for each of them is very comparable to the corresponding CO_2 desorption curve (Fig. 4c), suggesting CO and CO_2 share the same adsorption sites. In this regard, during CO_2 reduction, the in-situ produced CO intermediate can be stabilized, waiting to further hydrogenation to hydrocarbons. Moreover, CO and CO_2 adsorption capacity and intensity follows the same order: CCN > CCN-W > BCN. Considering that CO could be further converted to methane, ethylene and other hydrocarbon products, and moderate CO adsorption capacity and intensity is essential, it is expected that CCN-W is most suitable for selective photocatalytic CO_2 reduction to hydrocarbons.

3.3. Light absorption properties and band structures

Relative to BCN, CCN exhibit an evident enhancement in light absorption intensity in both UV and visible light regions and a slight red-shift in absorption edge (Fig. 5a), which could be attributed to the cooperative effects of stronger interlayer packing, extended covalent bonding in π-conjugated plane, and the K^+-doping in CCN [11,35]. Notably, after introducing W^{6+}-doping and associated localized impurity levels in the band gap, the absorption capacity in the visible light region is further enhanced for CCN-W, but the UV absorption is just slightly weakened because of enlarged interlayer distance after W^{6+}-doping (Fig. 2). The light absorption difference of CCN-W-X (X = 1, 2, 3) could further demonstrate this inference (Fig. S2).

The band structures were roughly estimated by combined optical and electrochemical analyses. First, the band gap energy (E_g) can be estimated from the corresponding Tauc plots (Fig. 5b) derived from the above UV–vis DRS spectra (Fig. 5a). The estimated E_g of BCN, CCN and CCN-W are 2.60, 2.53 and 2.39 eV, respectively. The Mott-Schottky plots (Fig. 5c) can be used to clarify the nature/type of the semiconductor and to estimate the flat band potentials (E_{fb}). The Mott-Schottky plots of all samples exhibit positive slopes, which is a typical characteristic of n-type semiconductors [2,50]. The E_{fb} of samples BCN, CCN and CCN-W are estimated to be − 1.53, − 1.33 and − 1.02 V versus the saturated Ag/AgCl (pH 6.7) reference electrode, respectively. It is widely accepted that the conduction band (CB) potential for n-type semiconductors is approximately more negative by 0.2 V as compared to that E_{fb} [34]. Meanwhile, the obtained potentials versus Ag/AgCl can be converted to the Normal hydrogen electrode (NHE) scale according to equations $E_{Ag/AgCl} = E_{RHE}$ - 0.059 pH - 0.197 and $E_{NHE} = E_{RHE}$ - 0.059 pH [51]. Thus, the CB potentials of samples BCN, CCN and CCN-W are calculated to be − 1.55, − 1.35 and − 1.04 V vs. NHE (pH 7) respectively. In combination with the value of E_g, the valence band (VB) potentials of samples BCN, CCN and CCN-W are calculated to be 1.05,
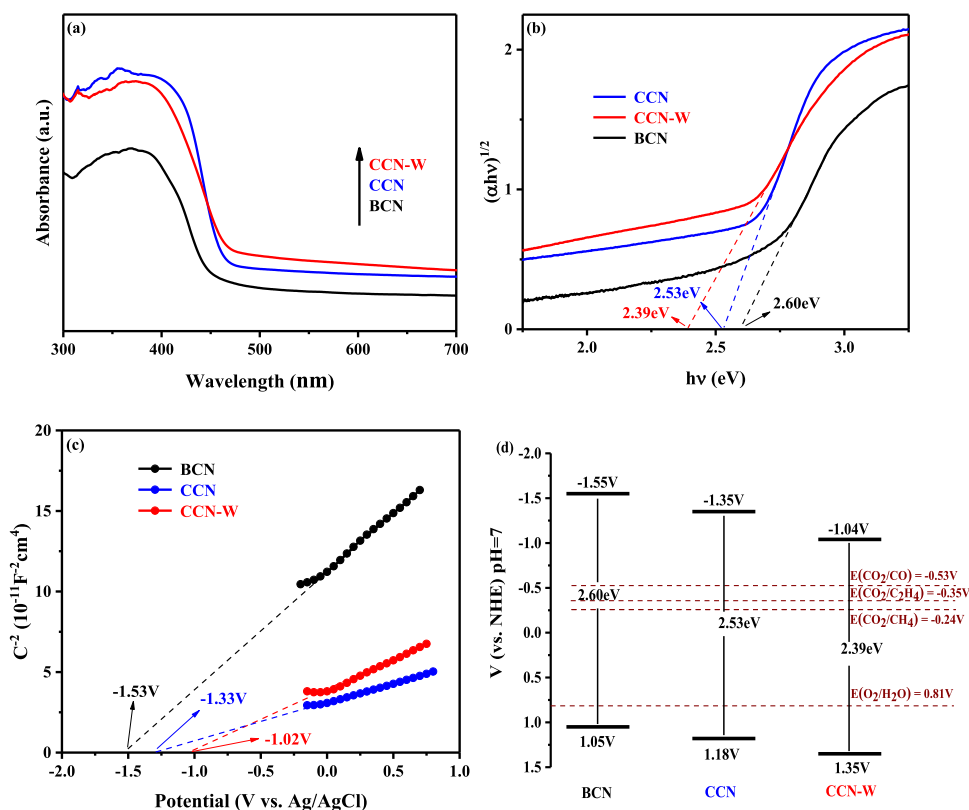

Fig. 5. UV–vis diffuse reflectance spectra (a), the plots of $(\alpha h\nu)^{1/2}$ vs. $(h\nu)$ for estimating E_g (b), the Mott-Schottky curves for estimating CB potentials (c) and the illustrated band structures (d) of samples BCN, CCN and CCN-W. α = the absorption coefficient; h = Planck's constant; ν = the light frequency.

1.18 and 1.35 V vs. NHE, respectively. The band structures for samples BCN, CCN and CCN-W are illustrated in Fig. 5d. The doping of M ions (M = K^+ or W^{6+}) in the cavity and forming M-N bonding will cause the charge redistribution of N atoms, affecting both CB and VB energy levels of CCN-W, because the N 2p orbitals of N atoms contribute to both the VB and CB [24]. Evidently, CB potentials of BCN, CCN and CCN-W follow the following order: BCN > CCN > CCN-W. Higher CB potential suggest stronger electron reduction ability. Even though, the CB potentials of CCN-W is far higher than the redox potential of diverse CO_2 reduction reactions (Fig. 5d). In contrast, the VB potentials of BCN, CCN and CCN-W follow the following order: BCN < CCN < CCN-W. Both CB and VB positions of CCN and CCN-W have been downshift compared to BCN, which are still thermodynamically feasible for the CO_2 reduction and the H_2O oxidation.

3.4. Charge dynamics

The steady state PL spectra (Fig. 6a) and the time-resolved PL spectra (Fig. 6b) are recorded to untangle the charge dynamic process. All the three sample show a typical steady-state PL emission peak at about 460 nm, which is close to the value of absorption edge (Fig. 5a). This PL peak can be mainly related to band-to-band recombination of photoelectrons and holes [32]. Obviously, the PL peak is substantially suppressed in CCN and CCN-W, relative to BCN. BCN possesses abundant terminal amino groups bonded by weak hydrogen bond within the π-conjugated plane, so the intralayer charge transport is greatly blocked by potential barrier of 7.9 eV [32]. Meanwhile, and interlayer distance of BCN is relatively larger because of weak van der Waals interlayer interaction, and the interlayer charge transfer is ever slower by even larger potential barrier of 33.2 eV [32]. Accordingly, the charge recombination possibility is very high in BCN, giving rise to strong PL signal. In contrast, in CCN, the terminal amino groups are mostly

removed, more covalent bonds are formed between adjacent heptazine units instead of hydrogen bonds. Moreover, after removing terminal amino groups, typical stacked sheet-like configuration extending along the 2D π-conjugated plane for BCN is evolved into rod-like morphology extending along c axis (perpendicular to 2D π-conjugated plane) for CCN (Fig. 1), the lateral dimension is greatly decreased and thus the diffusion lengths of photoelectrons from the interior to the lateral edges is shortened. Moreover, the interlayer interaction is strengthened by interlayer K^+-doping, resulting in reduced interlayer distance. All those aspects lead to faster charge transports and less charge recombination in CCN, yielding weak PL signal. After solvothermal-assisted W^{6+}-doping, while the aforementioned intralayer and interlayer structural merits of CCN are mostly remained, terminal cyano groups are largely removed, and additional $W-N_6$ centers are introduced to further promote the trapping and storage of photoelectrons, thus further reducing the charge recombination and weakening the PL signal in CCN-W. To gain a deeper insight into the charge transfer dynamics, the time-resolved PL decay spectra (Fig. 6b) are detected, which can be well fitted by triexponential functions (Text S1.4). The resulting time constants and relative amplitudes are listed in Table S3. The short lifetime (τ_1) corresponds to radiative exciton recombination, while the long lifetimes (τ_2 and τ_3) correspond to non-radiative recombination and energy-transfer process. Normally, faster exciton dissociation corresponds to lower exciton recombination and shorter exciton lifetime. BCN possesses the longest average exciton lifetime ($\tau_{ave.}$, 6.06 ns), suggesting the exciton dissociation is difficult in BCN, because of high charge localization within heptazine units connected by weak intralayer and interlayer intermolecular forces in BCN. In contrast, charge delocalization in CCN is greatly promoted by stronger intralayer and interlayer interactions, shorter the lateral inside-out charge transport distance, and abundant edge cyano groups and K^+-doping [7,18]. As a result, the exciton dissociation in CCN is greatly promoted, and the corresponding $\tau_{ave.}$ is reduced to
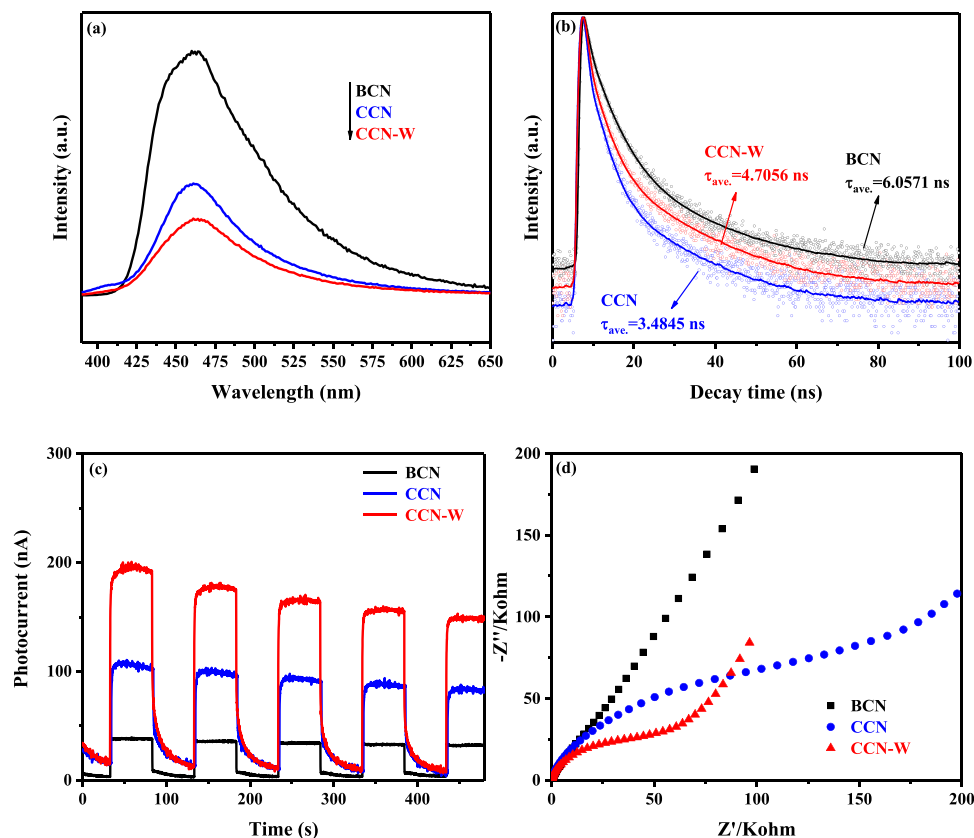

Fig. 6. The steady-state PL spectra (a), time-resolved PL spectra (b), transient photocurrent responses (c), and Nyquist plots of EIS spectra (d) of samples BCN, CCN and CCN-W.

3.48 ns. Upon solvothermal-assisted W^{6+}-doping, the $\tau_{ave.}$ for CCN-W (4.71) is slightly prolonged relative to CCN, which might be ascribed to slightly weakened interlayer interaction and partially lost edge cyano groups. Moreover, the introduced $W-N_6$ centers promote the trapping and storage of photoelectrons, retarding the electron delocalization. However, it is worthy to state that, those localized photoelectrons in $W-N_6$ centers would be mostly utilized in photocatalytic reaction systems, rather than recombination, owing to the cocatalyst effects of $W-N_6$ centers and higher charge utilization efficiency, which can be revealed clearly by the following electrochemical and photoelectrochemical tests.

The transient photocurrent and EIS analyses are performed to further study the charge transfer and utilization efficiency. The transient photocurrent response curves (Fig. 6c) were recorded for several on-off cycles under chopped light illumination. Limited by weak light absorption ability (Fig. 5a) and high exciton recombination possibility (Fig. 6a, b), the photocurrent density of BCN is the lowest (Fig. 6c). In comparison, owing the synergetic effects of greatly improved light absorption, inhibited exciton recombination and promoted exciton dissociation (charge delocalization) in CCN, more photoelectrons and holes are generated, and the photocurrent density of CCN is much higher than BCN. Interestingly, although the light absorption capacity and the radiative exciton recombination possibility of CCN-W is comparable to that of CCN, and the charge delocalization (exciton dissociation) dynamics in CCN-W is even restrained by the electron localization in $W-N_6$ centers, the photocurrent density of CCN-W is about 2 times higher than CCN. This result suggests that most photoelectrons localized in $W-N_6$ centers are not recombined but are utilized by the photoelectrochemical reactions on the photoelectrode surface. The charge transfer from catalyst surface to surface adsorbed O_2 molecules would be significantly enhanced in CCN-W, as evidenced by much lower O_2 desorption temperature in CCN-W than CCN (Fig. S3, O_2-TPD result). In this regard, the surface/interfacial charge transfer and utilization efficiency over CCN-W are greatly improved, leading to the much higher photocurrent density. This result is further demonstrated by the Nyquist plot of EIS spectra (Fig. 6d). The diameter of arcs in the semicircular Nyquist plot is corresponding to the charge transfer resistance (R_{ct}) across the electrode/electrolyte interface.[50] Obviously, the diameter of arcs in the Nyquist plot decreases in the following order: CCN-W < CCN < BCN, suggesting the lowest R_{ct} and the most efficient charge transfer efficiency in CCN-W, owing to the multiple modulation effects of solvothermal-assisted W^{6+}-doping in reducing charge recombination. Although the CCN possess stronger O_2 affinity (Fig. S3, O_2-TPD result), the cocatalyst role of $W-N_6$ centers in CCN-W facilitate the interfacial electron transfer from electrode surface to dissolved O_2 in electrolyte, reducing the R_{ct} of CCN-W.

In order to further examine the cocatalyst effects of $W-N_6$ centers, the electrocatalytic CO_2 reduction reaction (CO_2RR) on BCN, CCN and CCN-

W are evaluated through LSV spectra (Fig. 7a). All those samples show moderate CO_2RR activity, and relatively, CCN-W has the lowest onset potential and the highest current density. As demonstrated above, $W-N_6$ centers is helpful in activating CO_2 molecules with moderate adsorption affinity (Fig. 4). The present results highlight the cocatalyst role of $W-N_6$ centers in reducing reaction barrier and accelerating reaction efficiency. On the other hand, the electrocatalytic water oxidation reaction (WOR) on BCN, CCN and CCN-W are also evaluated through LSV spectra (Fig. 7b). The lowest onset potential for WOR over CCN-W indicates that WOR half reaction is also promoted by W^{6+}-doping. An efficient WOR is necessary in providing protons for hydrogenation steps during CO_2 reduction. Moreover, the efficient consumption of holes for WOR is also helpful in reducing charge recombination, not to mention that the WOR half reaction is dynamically rate-limiting step in water coupled CO_2 reduction reactions. As demonstrated in Fig. 5d, the band structures of g-C_3N_4 are regulated by W^{6+}-doping, giving rise to more positive VB level in CCN-W, offering photogenerated holes with stronger oxidation ability towards WOR half reaction.

3.5. Photocatalytic CO_2 reduction performance and mechanism

The photocatalytic CO_2 reduction performance of all samples are evaluated by water vapor-coupled photocatalytic CO_2 reduction experiments under the illumination of a 300 W full-spectrum Xenon lamp (320–780 nm). To avoid the competitive consumption of photoelectrons by O_2, the CO_2 conversion performance over the various samples are evaluated under anaerobic conditions. Control experiments indicate that both light irradiation and photocatalyst are indispensable for effective photocatalytic CO_2 reduction. For all the three samples, CO, CH_4 and C_2H_4 are generated as the main CO_2 reduction products (Fig. 8a), while the production of O_2 is also observed (inset of Fig. 8a) as the water oxidation product. The raw data of the GC signal for the main gas products (CH_4、CO and C_2H_4) from CCN-W are presented in Fig. S5a. To identify the carbon source of the detected reduction products, ^{13}C-isotope labeling experiments over CCN-W was monitored (Fig. S4). Luckily, the signal at $m/z = 17$ and $m/z = 29$ in the results are clearly recorded, which can be definitely assigned to $^{13}CH_4$ and ^{13}CO produced from $^{13}CO_2$, respectively. It indicates that the CO_2 was at least one of the dominant carbon sources to the recorded reduction products of CH_4 and CO. Unfortunately, the yield of C_2H_4 is below the detection limit (5 ppm) of GC-MS, so that it cannot be detected. As a supplement, control activity experiments are operated with CCN-W under the atmosphere of Ar versus CO_2 (Fig. S5b). Obviously, the amount of detected product under Ar atmosphere is far lower than that under CO_2 atmosphere. Considering that there may be remaining a small amount of residual air (containing trace CO_2 molecules) in the reactor after Ar purging, and that the CO_2 chemisorbed on the catalyst is difficult to be
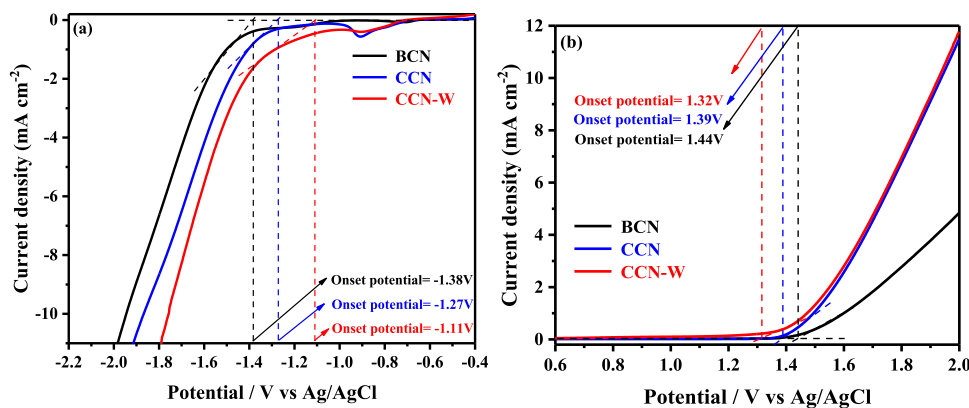

Fig. 7. Electrochemical CO_2 reduction (a) and H_2O oxidation (b) curves for samples BCN, CCN and CCN-W in CO_2-bubbled system, respectively. (The test undergoes in a 0.5 M Na_2SO_4 electrolyte.).
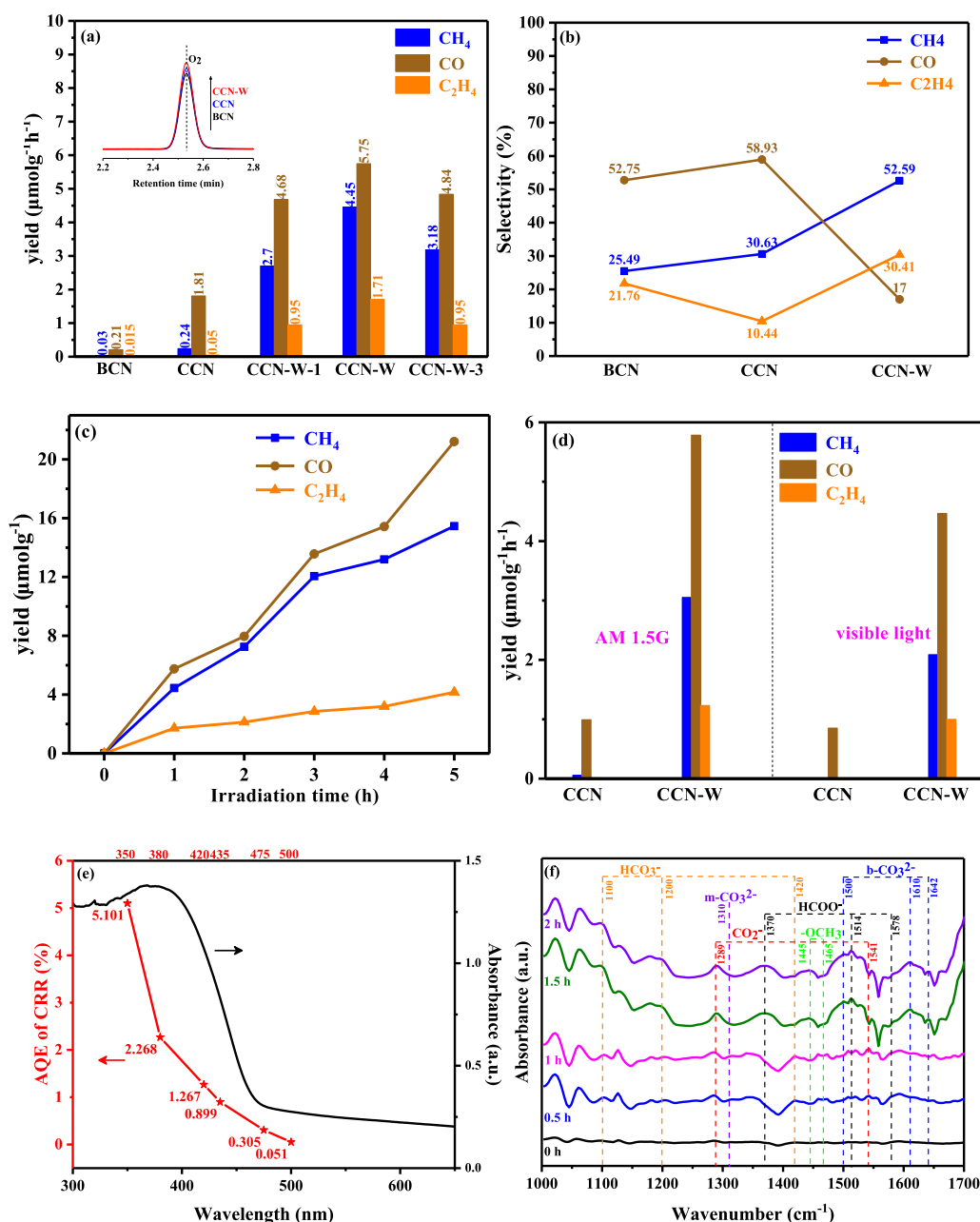
Fig. 8. The photocatalytic CO_2 reduction performances. (a) CO_2 reduction products obtained under full spectrum light Irradiation; (b) Selectivity of CO_2 reduction products based on utilization of photoelectrons. (c) CH_4, CO and C_2H_4 generation rates for CCN-W as a function of full spectrum irradiation time; (d) Comparison of the CH_4, CO and C_2H_4 generation rates for CCN and CCN-W obtained under visible-light and AM 1.5 G irradiation; (e) Wavelength-dependent CO_2 reduction of CCN-W under 1 h monochromatic light irradiation. (f) *In situ* DRIFTS spectra of surface adsorbed CO_2 species and photocatalytic CO_2 reduction intermediates on CCN-W under dark conditions (0–1 h) and under LED light irradiation (1–2 h).

completely removed under ambient conditions (Fig. 4c), it is not surprising there is still a small amount of CO and CH_4 produced, but almost no C_2H_4 can be detected. This comparative result further confirms that the photocatalytic products are mainly originated from CO_2 reduction.

As expected, the photocatalytic CO_2 reduction performance of CCN is much better than BCN, attributing to the improved light absorption, increased CO_2 chemisorption and higher density of photoelectrons. More importantly, the photocatalytic CO_2 reduction performance over CCN-W is even much better, and the CCN-W sample with optimized W^{6+}-doping level achieving the highest yields of CO (5.75 μmol g^{-1} h^{-1}), CH_4 (4.45 μmol g^{-1} h^{-1}) and C_2H_4 (1.71 μmol g^{-1} h^{-1}), totally (11.91μmol g^{-1} h^{-1}) being more than 5 times higher than that of CCN, with the yields of CO (1.81 μmol g^{-1} h^{-1}), CH_4 (0.24 μmol g^{-1} h^{-1}) and C_2H_4 (0.05 μmol g^{-1} h^{-1}). Moreover, as shown in Fig. 8b, the product selectivity of CH_4 (52.59%) and C_2H_4 (30.41%) for CCN-W, calculated based on the photoelectrons utilization percentage (see details in Text S1.5), are significantly improved. The overall selectivity of

hydrocarbons for CCN-W (83%) is more than 2 times higher than that for CCN (41.07%). The significantly improved activity and selectivity of CCN-W is ascribed to the multiple synergetic roles of introduced W-N$_6$ as active centers in gathering photoelectrons and CO_2 reactants, reducing reaction barrier and accelerating reaction efficiency, and stabilizing the CO intermediates moderately. The adsorption of CO intermediate on conventional g-C$_3$N$_4$ photocatalyst (BCN) is weak in adsorption strength, CO would be easily escaped from the catalyst surface. On the other hand, although the adsorption capacity and intensity of CO_2 and CO is quite strong on CCN, the photoelectrons cannot be enriched at the same active sites, and the CO hydrogenation is also restrained on CCN. As for CCN-W, the W-N$_6$ moieties act as active centers favor the adsorption of CO_2 and CO intermediate with moderate strength and coverage, and simultaneously, W-N$_6$ moieties enrich the photoelectrons, together favoring the yields of CH_4 and C_2H_4.

In addition, the stability of CCN-W is good enough, it still shows considerable photocatalytic CO_2 reduction performance after 5 h

illumination, and the yields of the major CO_2 reduction product are almost linearly increased with prolonging light illumination time (Fig. 8c). The basic structures and surface composition of the collected CCN-W after photocatalytic service is also well kept unchanged, which are confirmed by XRD, FTIR and XPS spectra (Fig. S6). The visible light photocatalytic CO_2 reduction performances (Fig. 8d) of CCN-W are also tested under the illumination of solely visible light (420–780 nm) and simulated natural solar light (AM 1.5 G, 200–1100 nm) at otherwise identical operation conditions. In both cases, the CCN-W performs much better, owing to the synergetic modulations in visible light absorption, photoelectron accumulation, CO_2 activation and reactions. Notably, the wavelength-dependent apparent quantum yields (AQE) of the photo-catalytic CO_2 reduction reactions over CCN-W are determined by utilizing different monochromatic lights (Fig. 8e). The highest AQE (5.10%) is achieved at wavelength of 350 nm, and the value of AQE is positively proportional to the wavelength-dependent light absorption capacity, further demonstrating that the present CO_2 reduction processes are dominated by the light absorption and excitation initiated photocatalytic reactions.

The reductive conversion of CO_2 involves complex participation of multiple electrons and protons, and the simultaneous breaking and forming of multiple covalent bonds. To disclose the possible CO_2 conversion process during photocatalytic reactions on the CCN-W photocatalyst, the in situ DRIFTS spectra (Fig. 8 f) have been implemented to detect the possible intermediates. The adsorbed CO_2 with different binding modes and the multiple CO_2 reduction intermediates, including carboxylate (CO_2^-, 1289 and 1541 cm^{-1}), bicarbonate species (HCO_3^-, 1100, 1200, 1420 cm^{-1}), monodentate carbonate species (m-CO_3^{2-}, 1310 cm^{-1}), bidentate carbonate species (b-CO_3^{2-}, 1500, 1610 and 1642 cm^{-1}), formate species ($HCOO^-$, 1370, 1514 and 1578 cm^{-1}), and methoxy groups (-OCH_3, 1445 and 1465 cm^{-1}), are detected in the present study [50,52]. Before light irradiation, CO_2^-, HCO_3^- and m-CO_3^{2-} species dominate, corresponding to the different adsorption modes. The CO_2 combined with surface hydroxyl (OH) groups could form surface HCO_3^-, while CO_2 bound to surface defects give rise to CO_2^- [50]. The chemisorption of CO_2 usually leads to the activation of CO_2 by changing the molecular geometry of the CO_2. After light irradiation, b-CO_3^{2-} species are intensified, meanwhile, $HCOO^-$ and -OCH_3 groups are appeared. It is suggested that bidentate adsorption of CO_2 molecules towards W-N_6 centers is promoted after light irradiation by enriching photoelectrons. $HCOO^-$ is a common intermediate during photocatalytic CO_2 reduction, which could be further transformed into CO. The surface bound CO could be released as final product, or undergo further hydrogenation to produce the hydrocarbons (Scheme 2), depending on the binding strength between CO intermediate and catalytically active sites. The detected -OCH_3 group is a key intermediate during the conversion of

CO_2 to CH_4. However, the characteristic intermediates to C_2H_4, related to C-C coupling, has not been detected. Based on theoretical calculation, the formation of C_2H_4 often involves two major steps: (1) CO_2 firstly converts to CO bound on the active centers; (2) The adjacent adsorbed CO undergoes further C-C coupling and hydrogenation to generate C_2H_4 [53].

BCN is characteristic of low degree of crystallinity, low specific surface area, high density of terminal amino groups and weak interlayer interaction (enlarged interlayer distance). The major drawbacks of BCN for photocatalytic CO_2 reduction lie in the following three aspects. First, the light absorption ability of BCN is relatively quite weak, especially in the UV regions (Fig. 5). Second, the CO_2 adsorption capacity is quite low (Fig. 4). Third, the density of available photoelectrons in BCN is low (Fig. 6). All those three aspects can be largely improved in CCN, because of the synergetic effects of reduced density of terminal amino groups, reduced interlayer distance (strengthened interlayer interactions), increased specific surface area, introduced K$^+$-doping (interlayer, cave and edge sites) and edge cyano groups. Nevertheless, although CO yield from photocatalytic CO_2 reduction on CCN is largely increased from 0.21 (BCN) to 1.81 (CCN) μmol g^{-1} h^{-1}, the CO selectivity was almost unchanged. The CO selectivity for CCN is 58.93% based on utilization percentage of photoelectrons (and the CO selectivity is 86.2% based on molar ratio of reduction products), which is comparable to that of BCN. Significantly, by W^{6+}-doping, CO selectivity can be greatly reduced to 17%, while the selectivity of hydrocarbons is increased to 83%, being 2 times higher than that of CCN. Moreover, the total yields of CO and hydrocarbons on CCN-W is increased by more than 5 times relative to CCN. Evidently, W^{6+}-doping and constructing W-N_6 as active centers in highly crystalline g-C_3N_4 nanorods is essential in improving the CO_2 reduction efficiency and selectivity simultaneously. The multiple synergetic effects (Scheme 2) are elaborated as follows:

First, the light absorption. CCN-W basically maintain the strong light harvesting ability as CCN. Relative to CCN, the light absorption capacity of CCN-W is not changed obviously after W^{6+}-doping, the UV absorption is slightly weakened, while the visible light absorption is slightly enhanced, which shall not be the major reason leading to the great performance improvement. Second, the charge dynamics. CCN-W and CCN have little difference in exciton recombination possibility (Fig. 6a) and exciton dissociation lifetime (Fig. 6b), and CCN-W performs even slightly worse in electron delocalization, because W-N_6 centers can accumulate and store photoelectrons by W^{6+}/W^{5+} cycling. The density of photoelectrons in CCN-W is about two times larger than CCN (Fig. 6c) and the charge utilization efficiency is improved by cocatalyst effects of W-N_6 centers, as evidenced by the lower interfacial charge transfer resistance (Fig. 6d) and lower redox reaction barrier (Fig. 7). Third, the CO_2 adsorption. Both CCN-W and CCN have considerable CO_2 and CO
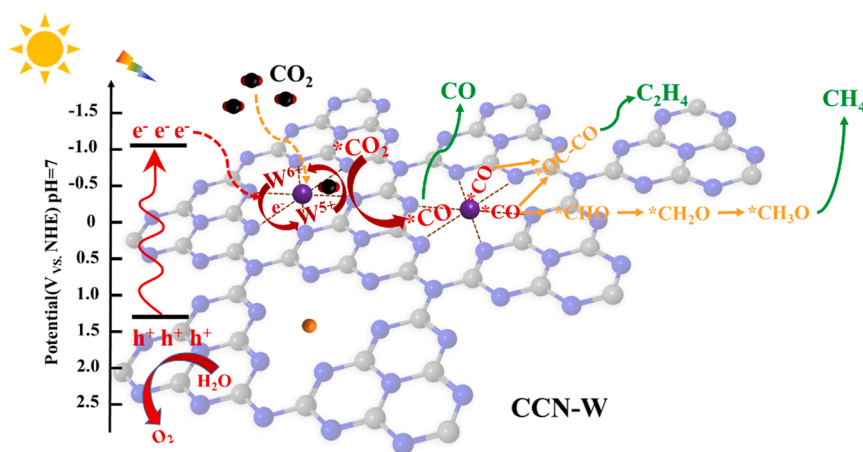
Scheme 2. Schematic illustration of the multifunctional role of W-N_6 active centers for photocatalytic CO_2 reduction over CCN-W.

adsorption capacity and strength. Relatively, the CO_2 adsorption capacity and intensity are higher in CCN. However, the moderate adsorption affinity of CCN-W is beneficial for CO_2 activation and reaction at lower potential barrier. Finally, the catalytic reactions. Both the photoelectrons and the CO_2 molecules can be enriched at the same W-N_6 active centers in CCN-W, being crucial in promoting the CO_2 reduction efficiency by high collision possibility and low CO_2 reduction reaction barrier (Fig. 7). In contrast, the CO_2 reduction dynamics in CCN would be compromised by random distribution of free photoelectrons. Moreover, the CO_2 reduction selectivity can be improved by in-situ stabilizing the CO intermediate at W-N_6 centers with moderate affinity. Combined together, both the CO_2 reduction efficiency and selectivity of CCN-W can be greatly improved by the multifunctional W-N_6 centers, which synergistically modulate the photocatalytic CO_2 reduction processes.

4. Conclusion

In summary, by solvothermal-assisted W-doping route, we have successfully prepared W-incorporated highly crystalline carbon nitride (CCN-W) nanorods photocatalyst for photocatalytic CO_2 reduction. The CCN-W with optimized W^{6+}-doping level exhibit excellent photocatalytic CO_2 reduction with CO、CH_4 and C_2H_4 yields of 5.75, 4.45, 1.71 $\mu molg^{-1}h^{-1}$, which are several times higher than those of BCN and CCN. Significantly, by W^{6+}-doping, CO selectivity can be greatly reduced to 17%, while the selectivity of hydrocarbons is increased to 83%, being 2 times higher than that of CCN. This study provides an excellent example for enhancing photocatalytic CO_2 reduction over CCN by synergetic modulation of W-N_6 active centers, which concentrate both the photoelectrons and CO_2 molecules, decrease energy barriers for CO_2 reduction, and tune the adsorption and activation of CO intermediate for promoting its following hydrogenation reaction. However, the mechanism of regulating the band structures of CCN-W after W^{6+}-doping and the generation path of multi-carbon products are still not clear enough, so the photocatalytic reduction process of the CO_2 should be further explored.

CRediT authorship contribution statement

Yujie Liang: Investigation, Writing – original draft; **Xi Wu**: Investigation; **Xueyan Liu**: Investigation; **Chuanhao Li**: Writing – review & editing; **Shengwei Liu**: Conceptualization, Supervision, Writing – review & editing, Funding acquisition.

Declaration of Competing Interest

The authors declare that they have no known competing financial interests or personal relationships that could have appeared to influence the work reported in this paper.

Acknowledgements

Appendix A. Supporting information

Supplementary data associated with this article can be found in the online version at doi:10.1016/j.apcatb.2021.120978.

References

[1] Q. Zhang, Y. Xia, S. Cao, "Environmental phosphorylation" boosting photocatalytic CO_2 reduction over polymeric carbon nitride grown on carbon paper at air-liquid-solid joint interfaces, Chin. J. Catal. 42 (2021) 1667–1676.

[2] S. Liu, F. Chen, S. Li, X. Peng, Y. Xiong, Enhanced photocatalytic conversion of greenhouse gas CO_2 into solar fuels over g-C_3N_4 nanotubes with decorated transparent ZIF-8 nanoclusters, Appl. Catal. B 211 (2017) 1–10.

[3] X. Wang, K. Maeda, A. Thomas, K. Takanabe, G. Xin, J.M. Carlsson, K. Domen, M. Antonietti, A metal-free polymeric photocatalyst for hydrogen production from water under visible light, Nat. Mater. 8 (2009) 76–80.

[4] M. Xiao, B. Luo, S. Wang, L. Wang, Solar energy conversion on g-C_3N_4 photocatalyst: light harvesting, charge separation, and surface kinetics, J. Energy Chem. 27 (2018) 1111–1123.

[5] Y. Li, M. Gu, X. Zhang, J. Fan, K. Lv, S.A.C. Carabineiro, F. Dong, 2D g-C_3N_4 for advancement of photo-generated carrier dynamics: status and challenges, Mater. Today 41 (2020) 270–303.

[6] W. Ren, J. Cheng, H. Ou, C. Huang, M.M. Titirici, X. Wang, Enhancing visible-light hydrogen evolution performance of crystalline carbon nitride by defect engineering, ChemSusChem 12 (2019) 3257–3262.

[7] L.H. Lin, H.H. Ou, Y.F. Zhang, X.C. Wang, Tri-s-triazine-based crystalline graphitic carbon nitrides for highly efficient hydrogen evolution photocatalysis, ACS Catal. 6 (2016) 3921–3931.

[8] H. Liu, D. Chen, Z. Wang, H. Jing, R. Zhang, Microwave-assisted molten-salt rapid synthesis of isotype triazine-/heptazine based g-C_3N_4 heterojunctions with highly enhanced photocatalytic hydrogen evolution performance, Appl. Catal. B 203 (2017) 300–313.

[9] W. Xing, W. Tu, Z. Han, Y. Hu, Q. Meng, G. Chen, Template-induced high-crystalline g-C_3N_4 nanosheets for enhanced photocatalytic H_2 evolution, ACS Energy Lett. 3 (2018) 514–519.

[10] L. Lin, Z. Yu, X. Wang, Crystalline carbon nitride semiconductors for photocatalytic water splitting, Angew. Chem. Int. Ed. 58 (2019) 6164–6175.

[11] G. Zhang, G. Li, Z.A. Lan, L. Lin, A. Savateev, T. Heil, S. Zafeiratos, X. Wang, M. Antonietti, Optimizing optical absorption, exciton dissociation, and charge transfer of a polymeric carbon nitride with ultrahigh solar hydrogen production activity, Angew. Chem. Int. Ed. 56 (2017) 13445–13449.

[12] Y. Xia, Z. Tian, T. Heil, A. Meng, B. Cheng, S. Cao, J. Yu, M. Antonietti, Highly selective CO_2 capture and its direct photochemical conversion on ordered 2D/1D heterojunctions, Joule 3 (2019) 2792–2805.

[13] Y. Li, F. Gong, Q. Zhou, X.H. Feng, J.J. Fan, Q.J. Xiang, Crystalline isotype heptazine-/triazine-based carbon nitride heterojunctions for an improved hydrogen evolution, Appl. Catal. B 268 (2020) 118381.

[14] Y. Li, D.N. Zhang, J.J. Fan, Q.J. Xiang, Highly crystalline carbon nitride hollow spheres with enhanced photocatalytic performance, Chin. J. Catal. 42 (2021) 627–636.

[15] J.Z. Zhang, C.Y. Yu, J.Y. Lang, Y.F. Zhou, B.X. Zhou, Y.H. Hu, M.C. Long, Modulation of Lewis acidic-basic sites for efficient photocatalytic H_2O_2 production over potassium intercalated tri-s-triazine materials, Appl. Catal. B 277 (2020), 119225.

[16] P. Xia, M. Antonietti, B. Zhu, T. Heil, J. Yu, S. Cao, Designing defective crystalline carbon nitride to enable selective CO_2 photoreduction in the gas phase, Adv. Funct. Mater. 29 (2019), 1900093.

[17] Y. Li, B. Li, D. Zhang, L. Cheng, Q. Xiang, Crystalline carbon nitride supported copper single atoms for photocatalytic CO_2 reduction with nearly 100% CO selectivity, ACS Nano 14 (2020) 10552–10561.

[18] Y. Li, D.N. Zhang, X.H. Feng, Q.J. Xiang, Enhanced photocatalytic hydrogen production activity of highly crystalline carbon nitride synthesized by hydrochloric acid treatment, Chin. J. Catal. 41 (2020) 21–30.

[19] J. Fu, K. Liu, K. Jiang, H. Li, P. An, W. Li, N. Zhang, H. Li, X. Xu, H. Zhou, D. Tang, X. Wang, X. Qiu, M. Liu, Graphitic carbon nitride with dopant induced charge localization for enhanced photoreduction of CO_2 to CH_4, Adv. Sci. 6 (2019), 1900796.

[20] B. Zhu, B. Cheng, L. Zhang, J. Yu, Review on DFT calculation of s-triazine-based carbon nitride, Carbon Energy 1 (2019) 32–56.

[21] H. Li, B. Zhu, S. Cao, J. Yu, Controlling defects in crystalline carbon nitride to optimize photocatalytic CO_2 reduction, Chem. Commun. 56 (2020) 5641–5644.

[22] F. Feng, W. Yang, S. Gao, L. Zhu, Q. Li, Photoinduced reversible lattice expansion in W-doped TiO_2 through the change of its electronic structure, Appl. Phys. Lett. 112 (2018), 061904.

[23] J. Ding, L. Wang, Q.Q. Liu, Y.Y. Chai, X. Liu, W.L. Dai, Remarkable enhancement in visible-light absorption and electron transfer of carbon nitride nanosheets with 1% tungstate dopant, Appl. Catal. B 176 (2015) 91–98.

[24] L. Zhu, X. Ma, N. Liu, G. Xu, C. Huang, Band structure modulation and carrier transport process of g-C_3N_4 doped with alkali metals, Acta Phys. Chim. Sin. 32 (2016) 2488–2494.

[25] Y. Gu, B. Xi, W. Tian, H. Zhang, Q. Fu, S. Xiong, Boosting selective nitrogen reduction via geometric coordination engineering on single-tungsten-atom catalysts, Adv. Mater. 33 (2021), e2100429.

[26] M. Kou, W. Liu, Y. Wang, J. Huang, Y. Chen, Y. Zhou, Y. Chen, M. Ma, K. Lei, H. Xie, P.K. Wong, L. Ye, Photocatalytic CO_2 conversion over single-atom MoN_2 sites of covalent organic framework, Appl. Catal. B 291 (2021), 120146.

[27] J. Wang, T. Heil, B. Zhu, C.W. Tung, J. Yu, H.M. Chen, M. Antonietti, S. Cao, A single Cu-center containing enzyme-mimic enabling full photosynthesis under CO_2 reduction, ACS Nano 14 (2020) 8584–8593.

[28] Y. Zheng, Y. Jiao, Y. Zhu, Q. Cai, A. Vasileff, L.H. Li, Y. Han, Y. Chen, S.Z. Qiao, Molecule-level g-C_3N_4 coordinated transition metals as a new class of

electrocatalysts for oxygen electrode reactions, J. Am. Chem. Soc. 139 (2017) 3336–3339.

[29] Z. Chen, J. Zhao, C.R. Cabrera, Z. Chen, Computational screening of efficient single-atom catalysts based on graphitic carbon nitride (g-C$_3$N$_4$) for nitrogen electroreduction, Small Methods 3 (2018), 1800368.

[30] B. Zhu, P. Xia, W. Ho, J. Yu, Isoelectric point and adsorption activity of porous g-C$_3$N$_4$, Appl. Surf. Sci. 344 (2015) 188–195.

[31] Z. Lou, Q. Gu, L. Xu, Y. Liao, C. Xue, Surfactant-free synthesis of plasmonic tungsten oxide nanowires with visible-light-enhanced hydrogen generation from ammonia borane, Chem. Asian J. 10 (2015) 1291–1294.

[32] Y. Kang, Y. Yang, L.C. Yin, X. Kang, L. Wang, G. Liu, H.M. Cheng, Selective breaking of hydrogen bonds of layered carbon nitride for visible light photocatalysis, Adv. Mater. 28 (2016) 6471–6477.

[33] G. Zhang, Y. Xu, D. Yan, C. He, Y. Li, X. Ren, P. Zhang, H. Mi, Construction of K$^+$ ion gradient in crystalline carbon nitride to accelerate exciton dissociation and charge separation for visible light H$_2$ production, ACS Catal. 11 (2021) 6995–7005.

[34] Y. Xie, Y. Zhuo, S. Liu, Y. Lin, D. Zuo, X. Wu, C. Li, P.K. Wong, Ternary g-C$_3$N$_4$/ZnNCN@ZIF-8 hybrid photocatalysts with robust interfacial interactions and enhanced CO$_2$ reduction performance, Sol. RRL 4 (2020), 1900440.

[35] S. Wu, H. Yu, S. Chen, X. Quan, Enhanced photocatalytic H$_2$O$_2$ production over carbon nitride by doping and defect engineering, ACS Catal. 10 (2020) 14380–14389.

[36] D.A.F. Goncalves, R.P.R. Alvim, H.A. Bicalho, A.M. Peres, I. Binatti, P.F.R. Batista, L.S. Teixeira, R.R. Resende, E. Lorencon, Highly dispersed Mo-doped graphite carbon nitride: potential application as oxidation catalyst with hydrogen peroxide, New J. Chem. 42 (2018) 5720–5727.

[37] K. Wu, D.D. Chen, J.Z. Fang, S.X. Wu, F. Yang, X.M. Zhu, Z.Q. Fang, One-step synthesis of sulfur and tungstate co-doped porous g-C$_3$N$_4$ microrods with remarkably enhanced visible-light photocatalytic performances, Appl. Surf. Sci. 462 (2018) 991–1001.

[38] W. Wang, H. Zhang, S. Zhang, Y. Liu, G. Wang, C. Sun, H. Zhao, Potassium-ion-assisted regeneration of active cyano groups in carbon nitride nanoribbons: Visible-light-driven photocatalytic nitrogen reduction, Angew. Chem. Int. Ed. 58 (2019) 16644–16650.

[39] W. Lin, K. Lu, S. Zhou, J. Wang, F. Mu, Y. Wang, Y. Wu, Y. Kong, Defects remodeling of g-C$_3$N$_4$ nanosheets by fluorine-containing solvothermal treatment to enhance their photocatalytic activities, Appl. Surf. Sci. 474 (2019) 194–202.

[40] J. Li, Xa Dong, Y. Sun, G. Jiang, Y. Chu, S.C. Lee, F. Dong, Tailoring the rate-determining step in photocatalysis via localized excess electrons for efficient and safe air cleaning, Appl. Catal. B 239 (2018) 187–195.

[41] J. Liu, C. Xiong, S. Jiang, X. Wu, S. Song, Efficient evolution of reactive oxygen species over the coordinated π-delocalization g-C$_3$N$_4$ with favorable charge transfer for sustainable pollutant elimination, Appl. Catal. B 249 (2019) 282–291.

[42] Z. Fang, D. Li, R. Chen, X. Huang, B. Luo, W. Shi, Multiple doped carbon nitrides with accelerated interfacial charge/mass transportation for boosting photocatalytic hydrogen evolution, ACS Appl. Mater. Interfaces 11 (2019) 22255–22263.

[43] J.J. Wu, N. Li, H.B. Fang, X.T. Li, Y.Z. Zheng, X. Tao, Nitrogen vacancies modified graphitic carbon nitride: scalable and one-step fabrication with efficient visible-light-driven hydrogen evolution, Chem. Eng. J. 358 (2019) 20–29.

[44] Q. Xie, W. He, S. Liu, C. Li, J. Zhang, P.K. Wong, Bifunctional S-scheme g-C$_3$N$_4$/Bi/BiVO$_4$ hybrid photocatalysts toward artificial carbon cycling, Chin. J. Catal. 41 (2020) 140–153.

[45] S. Zhang, Y. Zhuo, C.I. Ezugwu, C.C. Wang, C. Li, S. Liu, Synergetic molecular oxygen activation and catalytic oxidation of formaldehyde over defective MIL-88B (Fe) nanorods at room temperature, Environ. Sci. Technol. 55 (2021) 8341–8350.

[46] K.X. Li, L.S. Yan, Z.X. Zeng, S.L. Luo, X.B. Luo, X.M. Liu, H.Q. Guo, Y.H. Guo, Fabrication of H$_3$PW$_{12}$O$_{40}$-doped carbon nitride nanotubes by one-step hydrothermal treatment strategy and their efficient visible-light photocatalytic activity toward representative aqueous persistent organic pollutants degradation, Appl. Catal. B 156 (2014) 141–152.

[47] Y. Wang, Y. Zhang, S. Zhao, Z. Huang, W. Chen, Y. Zhou, X. Lv, S. Yuan, Bio-template synthesis of Mo-doped polymer carbon nitride for photocatalytic hydrogen evolution, Appl. Catal. B 248 (2019) 44–53.

[48] J. Wang, S. Cao, J. Yu, Nanocages of polymeric carbon nitride from low-temperature supramolecular preorganization for photocatalytic CO$_2$ reduction, Sol. RRL 4 (2019), 1900469.

[49] X. Wu, D. Gao, P. Wang, H. Yu, J. Yu, NH$_4$Cl-induced low-temperature formation of nitrogen-rich g-C$_3$N$_4$ nanosheets with improved photocatalytic hydrogen evolution, Carbon 153 (2019) 757–766.

[50] X. Liu, M. Ye, S. Zhang, G. Huang, C. Li, J. Yu, P.K. Wong, S. Liu, Enhanced photocatalytic CO$_2$ valorization over TiO$_2$ hollow microspheres by synergetic surface tailoring and Au decoration, J. Mater. Chem. A 6 (2018) 24245–24255.

[51] C. Yang, Q.Y. Tan, Q. Li, J. Zhou, J.J. Fan, B. Li, J. Sun, K.L. Lv, 2D/2D Ti$_3$C$_2$ MXene/g-C$_3$N$_4$ nanosheets heterojunction for high efficient CO$_2$ reduction photocatalyst: Dual effects of urea, Appl. Catal. B 268 (2020), 118738.

[52] X. Li, W. He, C. Li, B. Song, S. Liu, Synergetic surface modulation of ZnO/Pt@ZIF-8 hybrid nanorods for enhanced photocatalytic CO$_2$ valorization, Appl. Catal. B 287 (2021), 119934.

[53] K.D. Yang, C.W. Lee, K. Jin, S.W. Im, K.T. Nam, Current status and bioinspired perspective of electrochemical conversion of CO$_2$ to a long-chain hydrocarbon, J. Phys. Chem. Lett. 8 (2017) 538–545.